PCCP

ROYAL SOCIETY
OF CHEMISTRY

PAPER

View Article Online
View Journal | View Issue

Check for updates

Cite this: *Phys. Chem. Chem. Phys.*, 2024, **26**, 6736

An intrinsic electrical conductivity study of perovskite powders $MAPbX_3$ (X = I, Br, Cl) to investigate its effect on their photovoltaic performance†

Shafi Ullah, *[a] Andreu Andrio,[b] Julia Marí-Guaita,[a] Hanif Ullah,[c]
Antonio Méndez-Blas,[d] Roxana M. del Castillo Vázquez, [e] Bernabé Mari[a] and
Vicente Compañ *[f]

Received 22nd November 2023,
Accepted 26th January 2024

DOI: 10.1039/d3cp05686d

rsc.li/pccp

An investigation into the intrinsic electrical conductivity of perovskite powders $MAPbX_3$, where X represents iodine (I), bromine (Br), or chlorine (Cl), was conducted to explore its impact on their photovoltaic performance. Results revealed that $MAPbCl_3$ demonstrated light absorption ability in the ultraviolet and visible regions, while $MAPbBr_3$ showed capacity for light absorption at longer wavelengths in the visible spectrum. On the other hand, $MAPbI_3$ exhibited good absorption at longer wavelengths, indicating its ability to absorb light in the near-infrared region. The optical bandgap of each perovskite was determined to be 2.90 eV for $MAPbCl_3$, 2.20 eV for $MAPbBr_3$, and 1.47 eV for $MAPbI_3$. The electrical conductivities of these powders were measured in-plane using the four-probe method and through-plane by electrochemical impedance spectroscopy (EIS). Electrochemical impedance spectroscopy (EIS) studies revealed a significant change in the conductivity of the $MAPbI_3$ perovskite at temperatures between 80 °C and 100 °C. This change could be attributed to structural modifications induced when the temperature exceeds these values. The through-plane conductivity changed from 3×10^{-8} S cm^{-1} at 60 °C to approximately 6×10^{-5} S cm^{-1} at 120 °C and around 2×10^{-3} S cm^{-1} at 200 °C. Meanwhile, the sheet conductivity (in-plane conductivity) measurements performed at ambient temperature reveal that sheet conductivities are 489×10^3 S m^{-1}, 486×10^3 S m^{-1} and 510×10^3 S m^{-1} for $MAPbBr_3$, $MAPbCl_3$ and $MAPbI_3$, respectively. This study provides valuable insights for optimizing the performance of perovskite solar cells. Understanding how dopants influence the electrical conductivity and photovoltaic properties of the perovskite material, this work will enable researchers to design and engineer more efficient and stable solar cell devices based on $MAPbX_3$ perovskites.

1. Introduction

Over the past few years, there has been a remarkable advancement in optoelectronic devices utilizing hybrid organic/inorganic halide perovskites as active semiconductor materials.[1–3] Specifically, perovskite-based solar cells (PSCs) have achieved impressive efficiencies, reaching 25.2%, comparable to traditional silicon-based solar cells.[4] Additionally, there have been continuous improvements in the stability of these devices, indicating their potential for commercialization.[5,6] Despite the enthusiasm surrounding halide perovskites, their versatile processing methods, such as solution-based or evaporation techniques, are more complex compared to those used for organic semiconductors. The reason for this complexity lies in the close coupling between the actual crystallization of the perovskite material and its film formation. These two processes occur simultaneously and need to be optimized in parallel. This coupling contributes to the challenge of achieving consistent film formation and results in significant variations in device performance, even within the same laboratory. Such inconsistencies hinder the industrial adoption of perovskite-based devices.[7]

Addressing these challenges and improving the reproducibility of film formation are essential steps towards the

---

[a] *Instituto de diseño y Fabricación (IDF), Universitat Politècnica de València (UPV), Camino de Vera, s/n, 46022 Valencia, Spain. E-mail: Shafi399@yahoo.com*
[b] *Departamento de Física Aplicada, Universitat Jaume I, Avda. Sos Baynat, s/n, 12080-Castellón de la Plana, Spain*
[c] *Department of Electrical Engineering, Federal Urdu University (FUUAST), Islamabad, Pakistan*
[d] *Instituto de Física, Benemérita Universidad Autónoma de Puebla, Apartado Postal J-48, Puebla, 72570, Mexico*
[e] *Departamento de Física, Facultad de Ciencias, Universidad Nacional Autónoma de México (UNAM), DF, Mexico*
[f] *Departamento de Termodinámica Aplicada (ETSII), Universitat Politècnica de València, Camino de Vera, s/n, 46022 Valencia, Spain. E-mail: vicommo@ter.upv.es*

† Electronic supplementary information (ESI) available. See DOI: **https://doi.org/10.1039/d3cp05686d**

widespread adoption of perovskite-based optoelectronic devices in commercial applications. By better understanding and controlling the crystallization and film formation processes, researchers can enhance the performance and reliability of perovskite-based devices, ultimately paving the way for their successful integration into the market. Furthermore, the versatility of organic–inorganic hybrid perovskites extends beyond their impressive efficiencies, as their structural and optoelectronic characteristics can be readily adjusted through compositional engineering involving diverse organic ligands, metals, or halogens. This compositional variability has allowed researchers to utilize perovskites with different bandgap energies (E_g) in various applications, including wave-tunable lasing and light-emitting diodes.[8,9] Moreover, these tunable compositions have proven to be highly efficient in solar cell technology. Nevertheless, it is crucial to consider that the lattice of perovskites is highly sensitive to the size of coordinating organic cations. In cases where the cations are excessively large, two-dimensional (2D) layered perovskites with distinct semiconducting properties are formed.[10,11]

An alternative method for synthesizing halide perovskite powders, which does not involve the formation of layers, is the mechanochemical synthesis. Researchers have successfully demonstrated this procedure for various lead-containing and lead-free halide perovskite compositions.[12–15] The use of perovskite powders offers several advantages, such as superior storage stability, when compared to stock solution counterparts.[16] Additionally, dry synthesis approaches for perovskite powders expand the range of available reactants, as there are no solubility limitations.[17] The precise control of precursor stoichiometry in this method translates to better overall synthesis control, leading to improved device properties when converting the prepared perovskite powders into solution-based thin-films.[18–20] Moreover, the potential of halide perovskite powders is showcased in the demonstration of efficient X-ray detectors. These detectors were achieved by directly processing solution-based perovskite powders into a thick layer without the use of solvents, highlighting the versatility of these materials.[21]

The mechanochemical synthesis of perovskite powders shows promise, but there is still a lack of detailed understanding regarding the relationship between the properties of reactants, synthesis parameters, and the resulting structural and optoelectronic properties of the final perovskite powders. To address this gap, our study focuses on investigating two crucial aspects: the intrinsic conductivity of the mechanochemically synthesized perovskite powders and their ability to withstand external stress factors, such as temperature variations and frequency changes. These characteristics are significant when considering the potential commercial deployment of this synthesis method. By gaining insights into the conductivity and resilience of perovskite powders, we aim to shed light on their suitability and reliability for various practical applications.

In this regard, our research will primarily focus on studying the conductivity of perovskite powders of $MAPbX_3$, where X = I, Br and Cl, to understand how it affects the photovoltaic performance of these materials. To achieve this goal, we conducted in-plane conductivity measurements to determine the sheet resistivity of the perovskites and through-plane conductivity measurements by EIS to quantify the transversal conductivity.

In previous studies of our group, broadband dielectric spectroscopy has been employed to investigate the relationship between diffusivity, charge carrier density, and Debye length in relation to the structural dynamics of SILLPs.[22–24] Following a similar procedure, in this investigation, the influence of electrode polarization (EP) has been taken into account using a single Debye relaxation model, as demonstrated in the analysis conducted by Trukhan,[25] Sorensen *et al.*,[26] and MacDonald.[27–29] Following the same line of research as other researchers,[30–34] in this work, by incorporating the EP approach and fitting the peaks corresponding to the maximum of $\tan\delta$, we were able to determine the diffusivity, the mobility and charge carrier density of the various doping agents within the perovskite structure. These parameters provided insights into the cumulative process occurring in the system, resulting from interactions between charge carriers and mobile ions in the perovskites. From conductivity measurements, we will provide valuable insights into the behavior of the perovskite materials and its potential impact on enhancing their photovoltaic performance.

2. Experimental section

2.1. Synthesis of $MAPbX_3$ (X = I, Br, Cl) powders

All the starting materials were purchased from Sigma Aldrich and used as received without further purification. Perovskite crystal powders were synthesized by mixing an equimolar ratio of 0.30 mol CH_3NH_2 (33% in methanol) and the corresponding hydro halide acid HX (X = I, Br, Cl). The mixture was stirred for 2 hours in a 250 mL round-bottom flask, and the flask was kept in an ice bath at 0 °C. Subsequently, the mixture was heated to 100 °C for 30 minutes. A solution of 0.03 mol of $Pb(NO_3)_2$, previously dissolved in 50 mL of distilled water, was added dropwise to the hot MAX_3 (X = I, Br, Cl) solution under vigorous stirring.

Following this process, a precipitate of crystalline powders formed, exhibiting different colors: black for iodide, orange for bromide, and white for chloride. The remaining solution was allowed to cool to 50 °C and then filtered. The resulting crystalline powders were washed multiple times with absolute ethanol and diethyl ether. Finally, the powders were dried in an electric oven at 100 °C for 24 hours and then stored in a vacuum for further characterization.

The crystallographic properties of the synthesized samples were analyzed using X-ray diffraction (XRD) with a Rigaku Ultima IV diffractometer. Cu-Kα radiation with a wavelength (λ) of 1.5406 Å was used, and the measurements were conducted in the 2θ range from 10° to 60°, with a step size of 0.02°. For the examination of the sample's microstructure, transmission electron microscopy (TEM) measurements were carried out using a JEO-JEM-1010 instrument at 2.5 kV. To investigate the optical properties of the samples, absorption measurements were performed using an Ocean Optics HR4000 spectrophotometer equipped with a Si-CCD detector.

The measurements were taken within the wavelength range of 400 nm to 1000 nm.

2.2. Conductivity measurements

2.2.1. In-plane conductivity measurements. The four-probe method is commonly used to measure the sheet resistance of the material. In this method we calculate the apparent surface electrical resistance of the materials, named sheet resistance (R_s), by measuring the potential difference between the electrodes, as a consequence of the superficially circulating electric current (DC), applying Ohm's law.[35–37] According to the kit used to measure the resistance of the film by means of the four-point method, the value of R_s is given by.

$$R_s = 4.532 \times \frac{V}{I} \tag{1}$$

The constant 4.532 is introduced because of the geometry used in the measurement by the kit. Therefore, plotting the values of voltage and electric current we can easily calculate the sheet resistance from the slope. Then, knowing the sheet sample thickness, t, the in-plane resistivity ρ_s can be estimated from the sheet resistance R_s calculated using eqn (1) as

$$\rho_s = R_s \cdot t \tag{2}$$

Finally, the sheet conductivity (*i.e.*, in-plane conductivity) of perovskites can be obtained from the inverse of the sheet resistivity as

$$\sigma_s = \frac{1}{\rho_s} \tag{3}$$

where ρ_s is the sheet resistivity, which is usually expressed in terms of the International Annealed Copper Standard (%IACS). The value of 100% IACS is defined as the electrical conductivity corresponding to a volume resistivity of 17.241 nΩ m = 58 MS m^{-1} at 20 °C.

2.2.2. Through plane conductivity measurements. Electrochemical impedance spectroscopy (EIS) measurements were carried out to measure the transversal conductivity of the perovskite powders in a vacuum cell. For this, the powders were compressed into pellets and the average thickness was determined by taking the average of various measurements in different surface planes using a micrometer. Besides, the samples were inserted between two gold electrodes attached to the impedance spectrometer working as blocking electrodes. The conductivity of the powders in the cross path was assessed using a Novocontrol broadband dielectric spectrometer (BDS) (Hundsangen, Germany) combined with an SR 830 lock-in amplifier with an Alpha dielectric interface by following the same procedure described earlier,[38–40] in the frequency range of $10^{-1} < f < 10^7$ Hz utilizing a 0.1 V signal amplitude in a range of temperature between 20 and 200 °C in steps of 20 °C. The temperature was kept constant with a stepwise range of 20 °C from 20 to 200 °C controlled by a nitrogen jet (QUATRO from Novocontrol) with a temperature inaccuracy of 0.1 K during every single stretch in frequency. For this, we have followed the same procedure previously used by our research group. Initially, a temperature sequence from 20 °C to 200 °C and then from 200 °C to 20 °C, in steps of 20 °C, was used. Later, in a new cycle of temperature scan, the dielectric spectra were accumulated in each stage from 20 to 200 °C, and this cycle is called the drying cycle. This was achieved with the intention to exclude possible molecules of water in the perovskites.

3. Results and discussion

3.1 XRD analysis

The preparation of perovskite powders of $MAPbX_3$, (X = I, Br, or Cl) was carried out as described above in the experimental section. These perovskite powders exhibit good solubility in polar organic solvents, including *N*-methyl-2-pyrrolidinone (NMP), *N*,*N*-dimethylacetamide (DMAC), *N*,*N*-dimethylformamide (DMF), and dimethyl sulfoxide (DMSO). In Fig. 1, optical images of the synthesized $MAPbX_3$ perovskite powders are presented, along with their corresponding X-ray diffraction (XRD) spectra. The colors of the synthesized powders are observed as follows: black for $MAPbI_3$, bright orange for $MAPbBr_3$, and almost colorless and transparent for $MAPbCl_3$. The XRD spectra exhibit characteristic peaks that align well with those reported in the literature.[41–44]

The XRD analysis highlights that the three halides $MAPbX_3$ share a consistent phase, free from secondary contributions like MAX or PbX_2. Notably, $MAPbI_3$ adopts a tetragonal crystal structure, while the remaining films conform to a cubic perovskite structure. The lattice parameters follow a decreasing sequence of I, Br, and Cl. This results in a distinct shift of the (200) peak towards higher diffraction angles ($MAPbI_3$: 28.70°, $MAPbBr_3$: 30.36°, and $MAPbCl_3$: 31.69°), aligning with both anticipated outcomes and the existing literature. Fig. 1 visually compares the final XRD measurements for the three deposited samples.

Additionally, the powder X-ray diffraction patterns of all three synthesized compounds confirm the presence of phase-pure

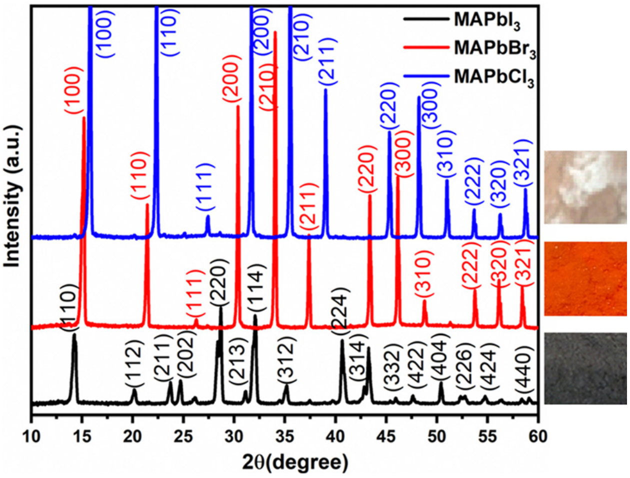

Fig. 1 X-ray diffractograms of $MAPbX_3$ (X = I, Br, Cl) along with optical images of perovskite powders.

Table 1 Lattice parameters, crystal systems, and space groups of MPX_3 samples[46,47]

System	Space group	Crystal system	*a*, Å	*b*, Å	*c*, Å
$MAPbI_3$	*I4cm*	Tetragonal	8.819(2)	8.819(2)	12.634(5)
$MAPbBr_3$	*Pm3m*	Cubic	5.875(8)	5.875(8)	5.875(8)
$MAPbCl_3$	*Pm3m*	Cubic	5.675(4)	5.675(4)	5.675(4)

products. Specifically, $MAPbI_3$ exhibits a tetragonal structure, while both $MAPbBr_3$ and $MAPbCl_3$ crystallize in a cubic structure, as detailed in Table 1. These structures correspond to the room-temperature configurations previously reported for these materials.[45] Besides, the quantitative XRD results are supported by TEM and HRTEM characterization.

3.2 TEM study

Fig. 2 presents the results of High-Resolution Transmission Electron Microscopy (HRTEM) used to closely examine the nanostructures of $MAPbX_3$ (X = I, Br, and Cl) perovskite powders. To conduct the analysis, the powders were dispersed and deposited onto a lacey carbon copper grid. HRTEM images were collected from various areas of the samples, and the findings revealed high crystalline quality, indicating the absence of planar or extended defects in all the studied samples (Fig. 2a–c). In Fig. 2a, an HRTEM image provides an overview of the nanostructure of $MAPbI_3$ perovskite powder. The presence of crystallites with different orientations is clearly visible. In higher electron-transparent regions, well-defined atomic columns are observed. Furthermore, the HRTEM images in Fig. 2a display lattice fringes with a spacing of 0.55 nm, corresponding to the *d*-spacing (114, 222) planes of the tetragonal $MAPbI_3$ structure. These observations align with previous findings reported in the existing literature.[48,49]

Similarly, Fig. 2b depicts the HRTEM image of the $MAPbBr_3$ perovskite powder, exhibiting a lattice spacing of 0.40 nm, which uniquely matches the interplanar distance of the (200) plane in the cubic $MAPbBr_3$ structure. This finding is consistent with data obtained from XRD experiments.[50] Moreover, the HRTEM image of the $MAPbCl_3$ sample in Fig. 2c reveals a separation of 0.90 nm. These results indicate the interplanar distance of the (110) plane in the cubic phase of the $MAPbCl_3$ structure and the (211) plane of the orthorhombic secondary phase of $PbCl_2$.

Overall, the HRTEM analysis of the $MAPbX_3$ perovskite powder samples has provided valuable insights into their nanostructure, crystal quality, and crystallographic information. These findings are essential for a comprehensive understanding of the properties and potential applications of these perovskite materials.

3.3 Optical results

In Fig. 3 the UV-visible spectra of the perovskite powders are displayed to investigate the optoelectronic properties of these materials, revealing distinct absorption onsets for each composition. Specifically, $MAPbCl_3$ exhibits a sharp absorption onset at 427 nm, indicating its ability to absorb light in the ultraviolet and visible regions, while $MAPbBr_3$ shows an absorption onset at 563 nm, showing its capacity to absorb light at longer wavelengths in the visible spectrum. Lastly, for $MAPbI_3$, the absorption onset occurs at a longer wavelength of 843 nm, indicating its ability to absorb light in the near-infrared region. These absorption onset values correspond to the optical bandgap (E_g) of each perovskite

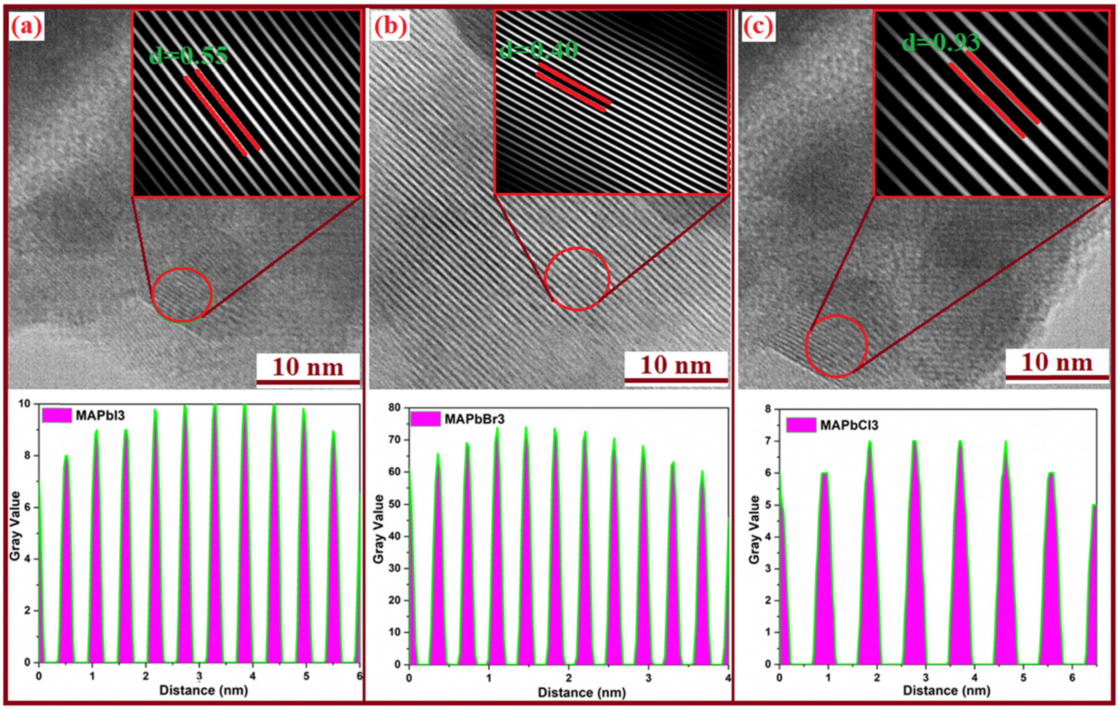

Fig. 2 (a)–(c) HR-TEM images of $MAPbX_3$ (X = I, Br and Cl) perovskites along with the corresponding shell layer distance images.

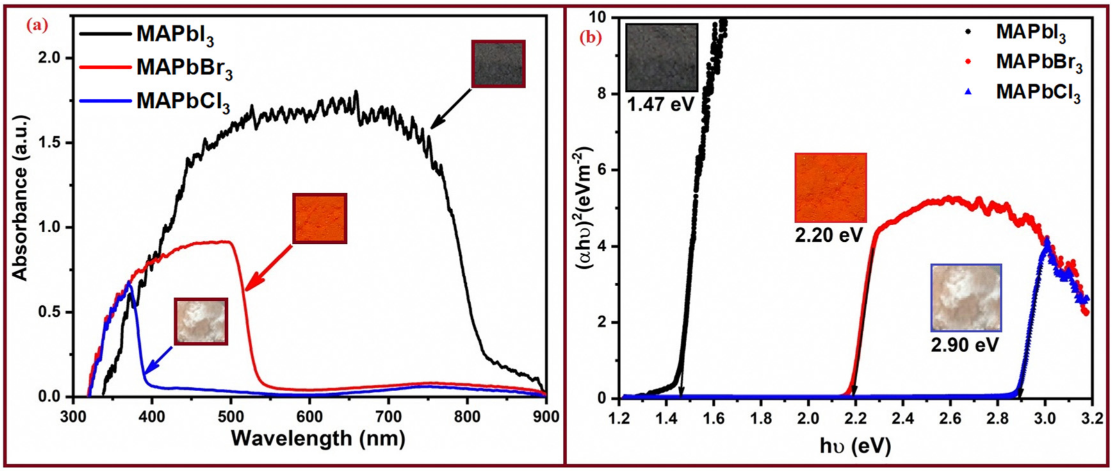

Fig. 3 (a) The UV-visible absorption spectra of the three perovskite powders and (b) their corresponding optical bandgap values.

composition. The calculated optical bandgap values are as follows: 2.90 eV for $MAPbCl_3$, 2.20 eV for $MAPbBr_3$, and 1.47 eV for $MAPbI_3$.

These optical bandgap values are crucial for understanding the energy levels and electronic properties of perovskite materials, with significant implications for their potential applications in optoelectronic devices, such as solar cells and light-emitting devices. In our study, we observed that $MAPbI_3$ with the optical band gap value of 1.47 eV represents the optimal perovskite material for solar photoelectric energy conversion devices, compared to the other materials analyzed, which had band gaps of 2.20 eV and 2.90 eV, respectively, calculated from their absorption spectra. These values are higher than the band gaps observed in the case of Cr-doped CIGS, which had values of around 1.15–1.20 eV.[51] Conversely, our obtained values precisely adhere to the patterns established in the existing literature, confirming that our determined energy band gap falls within the perovskite range.[47]

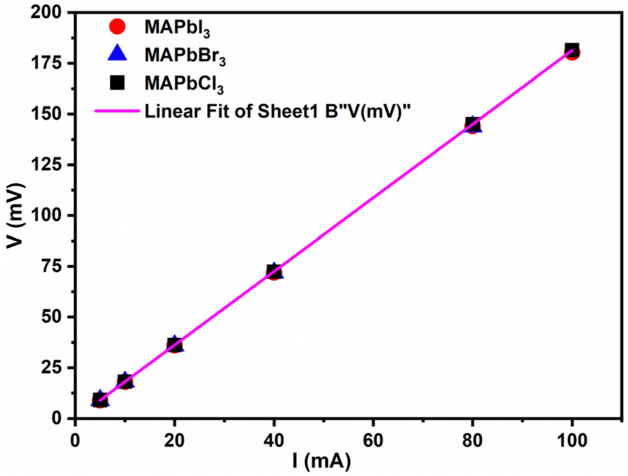

Fig. 4 The fluctuation of the potential between the electrodes in response to a given current intensity for thin film samples of $MAPbBr_3$, $MAPbCl_3$, and $MAPbI_3$, at ambient temperature. The lines within the graph depict the fitting of the experimentally obtained values.

3.4. Analysis of the conductivity

3.4.1. In-plane conductivity measurements. The electrical properties of perovskites were studied using the four-probe method. According to this method in which four probes are arranged equidistantly in a straight line and pushed against the film, the sheet resistivity may be calculated through determining the potential difference between the voltage-electrodes, due to current passing *via* an easily identifiable connection between the two current-electrodes, as reported in other studies.[35–37] According to the kit used to measure the resistance of the film by means of the four-point method, the value of ρ_s is determined from the sheet resistance R_s calculated using eqn (1). The results obtained for the three samples, measured at ambient temperature, are given in Fig. 4, where the fluctuation of the potential between the electrodes in response to a given current intensity applied has been plotted. A close inspection of these figures allows us to observe that the sample resistance (R_s) of the films remains constant, and its values can be obtained from the slope of the experimental fit determined from the plot of voltage *versus* intensity. A clear linearity is observed for all the samples, and the slope is approximately 1.8 Ω.

Knowing the sheet sample thickness (t), the in-plane apparent resistivity (ρ_s) of the perovskites, commonly named the sheet resistivity, was obtained from eqn (2), and the sheet conductivity was calculated from the inverse of the sheet resistivity, as indicated in eqn (3). The results obtained are given in Table 1.

On the other hand, from both Fig. 4 and Table 2, we can observe that the perovskites exhibit quite similar sheet resistance as the slopes of the straight lines for the three samples are practically the same. The values of the sheet resistivity obtained for the perovskites expressed in terms of the International Annealed Copper Standard (%IACS) are about 0.1% IACS. The values of in-plane conductivity (σ_s) of all perovskites are 489×10^3 S m^{-1}, 486×10^3 S m^{-1} and 510×10^3 S m^{-1} for $MAPbBr_3$, $MAPbCl_3$ and $MAPbI_3$, respectively. Considering that 100% IACS is defined as the conductivity corresponding to a

Table 2 The electrical properties of the perovskites determined at ambient temperature using the four-probe method

Samples	Thickness (nm)	Sheet resistivity (ρ_s) (nΩ m)	Sheet resistance (R_s) (Ω)	Sheet conductivity (σ_s) × 10^{-3} (S m^{-1})
$MAPbBr_3$	251 ± 12	2046 ± 18	8.15 ± 0.02	489 ± 4
$MAPbCl_3$	255 ± 14	2058 ± 16	8.07 ± 0.02	486 ± 4
$MAPbI_3$	240 ± 10	1961 ± 15	8.17 ± 0.02	510 ± 3

volume resistivity of 17.241 nΩ m at 20 °C, these values are around 86 times lower than that obtained for the TiB_{2p}/Cu composite powder prepared by the *in situ* reaction in combination with rolling, which were measured using a Sigma 2008B eddy current conductivity instrument.[52]

Focused Ion Beam (FIB) was employed to ascertain the cross-sectional profile of the thin films, which is consistent with the literature, measuring approximately 250 nm. All three samples have almost the same thickness because we are using the same parameters for deposition through the spin coating technique. Furthermore, our results match the existing literature.[53]

3.4.2. Electrochemical impedance spectroscopy (EIS) analysis. The through plane ionic conductivity (*i.e.*, the transversal conductivity) of the perovskites sample powders, $MAPbBr_3$, $MAPbCl_3$ and $MAPbI_3$, (σ_{dc}), was determined following two different methods: (1) from the Nyquist plot obtained using a Novocontrol broadband dielectric spectrometer, where a blocking electrode configuration was maintained in the cell where the sample was sandwiched between two electrodes in the entire temperature range studied. The results obtained are plotted in Fig. 5, where the plot of the real and imaginary parts of the complex impedance, Z'' (Ω) *vs.* Z' (Ω), displays typical semicircles where two well defined regions are detected. On the one hand, a high frequency depressed semicircle is followed by an accumulation of points when the imaginary part of the impedance tends to zero, which is the case of the sample $MAPbI_3$ at low and moderate temperatures. At high temperatures, we can observe that in the region of high frequencies the semicircle does not end at the origin of coordinates since the value of the complex impedance is still high and practically of the same order of magnitude as the real part of the impedance. However, this does not happen in the case of the other two samples, where complete semicircles are observed in the entire range of temperatures studied, although in the case of the sample with Cl_3 the possible existence of a second semicircle in the low frequency region seems to be observed.

The modelling of experimental data represented in the Nyquist plot shown in Fig. 5 was obtained from the equivalent circuit

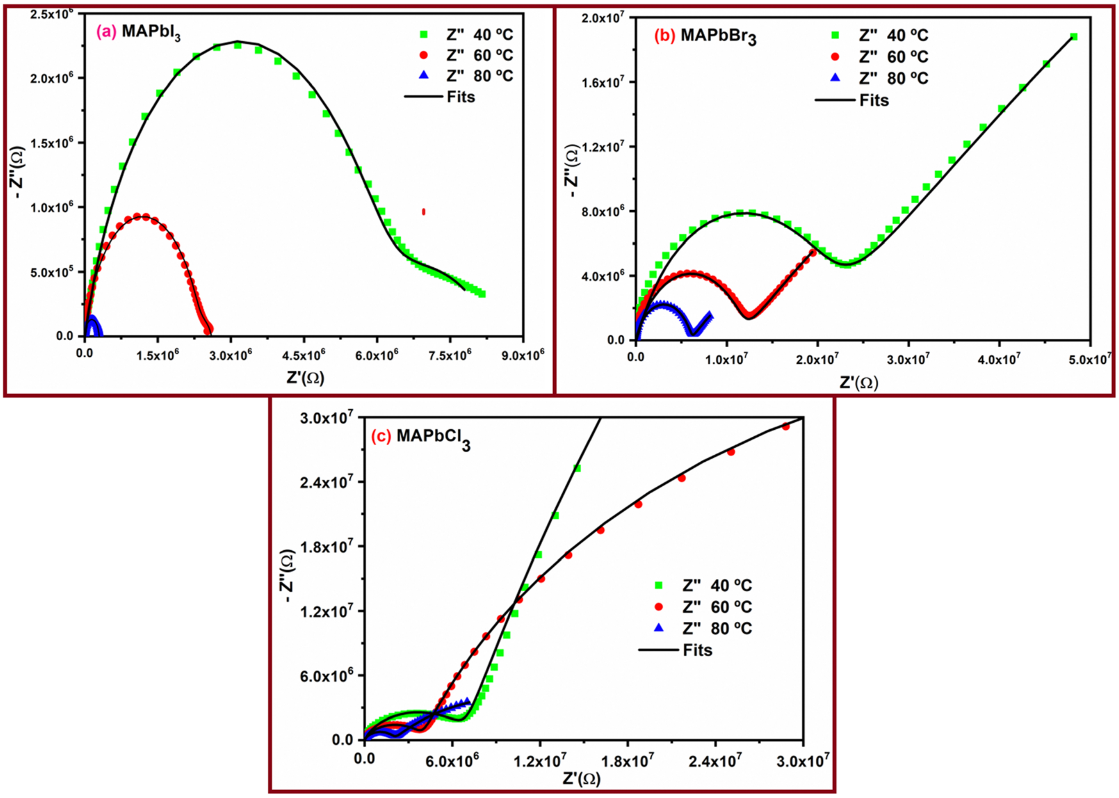

Fig. 5 Nyquist plots representing the complex impedance *vs.* real part of the impedance, at various temperatures (40 °C, 60 °C and 80 °C) for the $MAPbI_3$ sample (a), $MAPbBr_3$ sample (b) and $MAPbCl_3$ sample (c), respectively. The solid lines represent the fits of eqn (5) to the experimental data. Nyquist plots for the other temperatures are given in Fig. SI2, SI3 and SI4 of ESI.†

shown in ESI† (Fig. SI1). This equivalent circuit is formed by a parallel combination of a resistance R1 and a constant phase element (CPE1), the sub-circuit (R1-CPE1), in series with a parallel resistance (R2) with a constant phase element (CPE2), the sub-circuit (R2-CPE2), where the impedance of the CPE is identified from the expression.

$$Z_{\mathrm{CPE}_i} = \frac{1}{Q_i (j\omega)^{\alpha_i}} \tag{4}$$

where ω is the frequency, Q_i denotes the proportional factor, and α_i indicates the capacitive nature of the perovskites and lies between 0 and 1, and j is the imaginary unity ($j = (-1)1/2$). Then, in this model the complex impedances will be given by eqn (5), which fits very well with our experimental data, as we can see in Fig. 5.

$$Z_i^*(\omega) = R + \sum_i \frac{R_i}{1 + R_i Q_i (j\omega)^a} \tag{5}$$

In Table 3 we can see the parameters R, R_1, R_2, Q_1, Q_2, α_1, and α_2, determined using the equivalent circuit fitted following expression (5). Considering that the relation between complex impedance and complex conductivity is given by,

$$\sigma^*(\omega, T) = \frac{L}{A \cdot Z^*(\omega, T)} \tag{6}$$

the real part of the conductivity (σ'), named direct current conductivity (σ_{dc}), can be obtained from eqn (6) when the imaginary part of the complex impedance $Z''(\omega,T)$ is zero, then,

$$\sigma'(\omega, T) = \frac{L}{A \cdot Z'(\omega, T)} \tag{7}$$

In our study, the powder sample thickness was measured using a micrometer, with values being 561 ± 17 μm, 672 ± 20 μm, and 291 ± 10 μm for $MAPbBr_3$, $MAPbCl_3$ and $MAPbI_3$, respectively, and the area of the sample sandwiched between the two electrodes is $A = 0.785\ \mathrm{cm}^2$, and we can determine the values of the conductivity at each temperature by the determination of the real part of the impedance, $Z'(\omega,T)$.

Conductivity values obtained for the powders $MAPbI_3$, $MAPbBr_3$ and $MAPbCl_3$ following the Cole–Cole plots shown in Fig. 5 are given in the last column in Table 1. For this, we have considered the equivalent circuit displayed in Fig. SI1 (ESI†) and eqn (5) to simulate the experimental results and obtain the parameters R, R_1 and R_2, given in Table 3. Notice that the value of R determined in all the fits was zero ($R = 0$). From the values obtained for the resistances, the values of conductivity were calculated using eqn (7), where $Z'(\omega,T)$ is equal to ($R_1 + R_2$). In the last column of Table 3 we have gathered the values of the conductivities obtained for the samples $MAPbI_3$, $MAPbBr_3$ and $MAPbCl_3$, respectively.

A close inspection of Fig. 5 shows the existence of a different behavior of the sample $MAPbI_3$ than $MAPbBr_3$ and $MAPbCl_3$, respectively. This can be due to the grain boundary polarization as a highly capacitive phenomenon, which is characterized by larger relaxation times than the polarization mechanism in the bulk where the behavior of the grains is similar to that of a semiconductive material, and such a phenomenon is more apparent in the sample $MAPbI_3$ than in $MAPbBr_3$ and $MAPbCl_3$, respectively. This fact usually results in the appearance of two separate arcs in the Z'' *versus* Z' plots, one representing the bulk effect at high frequencies, while the other representing the surface effect in the lower frequency range. The complex impedance spectrum was interpreted for all the samples by means of the equivalent circuit shown in Fig. SI1 (ESI†). There are cases where the experimental data exhibit a spike at low frequencies, typically occurring at lower temperatures of around 20 and 40 °C. As observed, all the spectra demonstrate a prominent arc wherein a segment of the semicircle intercepts at the origin of coordinates at higher frequencies ($R = 0$), while the other segment either intercepts or tends to approach intercepting as Z'' approaches zero, giving R_1 and R_2 at each temperature. Utilizing these values, we have calculated the perovskite conductivity. This is achieved by considering the effective area of the sample, which is equivalent to the area of the sample situated between the two electrodes ($S = 0.785\ \mathrm{cm}^2$), along with its thickness (L). In our study, the powder sample thicknesses measured using a micrometer were 561 ± 17 μm, 672 ± 20 μm, and 291 ± 10 μm for $MAPbCl_3$, $MAPbBr_3$, and $MAPbI_3$, respectively.

The outcomes derived from the Nyquist plot, which were employed to ascertain the sample's resistance, were further subjected to eqn (7) to determine the direct current conductivity (σ_{dc}) at specific temperatures. These calculated values are listed in the column specified by σ (S cm^{-1}) in Table 3. It is crucial to note that this approach is considered an indirect method because the determined resistance is contingent on the criteria of the chosen equivalent circuit.

From Table 3 we can see that in the entire range of temperatures studied, the conductivity values follow the trend $\sigma_{\mathrm{MAPbCl_3}} < \sigma_{\mathrm{MAPbBr_3}} < \sigma_{\mathrm{MAPbI_3}}$. These values vary between 10^{-9} and 10^{-3} S cm^{-1} for $MAPbI_3$, between 10^{-10} and 10^{-6} S cm^{-1} for $MAPbCl_3$, and between 10^{-9} and 10^{-5} S cm^{-1} in the case of $MAPbBr_3$. These values were determined between 20 and 200 °C, respectively. All these values were similar to or even higher than the values reported by Leupold *et al.*[55] in the study carried out on the electrical conductivity as a function of the iodine partial pressure of powder aerosol deposited $MAPBI_3$ calculated from impedance spectra, as is done in this study.

The differences observed in conductivity, based on the type of dopant, can be attributed to variations in the concentration of mobile charges. Furthermore, their mobility is influenced by the strength of interactions with different stages of perovskites at various temperatures. A thorough investigation of this aspect will be conducted beforehand.

In Fig. 6 are plotted the conductivity values tabulated in Table 3 obtained for the different perovskites in the entire range of temperatures studied.

Fig. 6 distinctly illustrates the relationship between conductivity and temperature. A close inspection of Fig. 6 shows that the temperature dependence of the conductivity of perovskites exhibits an Arrhenius behavior in the entire range of

Table 3 Parameters R_1, R_2, Q_1, Q_2, α_1 and α_2 extracted by fitting experimental results using the equivalent circuit described in eqn (5) to the Nyquist diagrams obtained for the samples $MAPbI_3$, $MAPbBr_3$ and $MAPbCl_3$, respectively. r^2 represents the coefficient of determination of the fittings and σ the electrical conductivity. The expression for r^2 is $r^2 = 1 - \frac{\sum_{i=1}^{N}(y_i - \hat{y}_i)^2}{\sum_{i=1}^{N}(y_i - \bar{y})^2} = 1 - \frac{{\sigma_r}^2}{{\sigma_y}^2}$, where y_i is the measured data set, $\hat{y}_i$ is the modelled data set, $\bar{y}$ is the mean of the measured data, ${\sigma_r}^2$ is the residual variance and ${\sigma_y}^2$ is the variance[54]

Samples	T (°C)	R_1 (Ω)	Q_1	α_1	R_2 (Ω)	Q_2	α_2	r^2	σ (S cm^{-1})
$MAPbI_3$	20	6.0×10^{7}	9.5×10^{-10}	0.77	4.1×10^{7}	7.5×10^{-9}	0.35	0.900	3.7×10^{-9}
	40	5.9×10^{6}	4.3×10^{-10}	0.81	2.6×10^{6}	17×10^{-8}	0.45	0.996	4.4×10^{-8}
	60	2.4×10^{6}	1.6×10^{-10}	0.85	2.5×10^{5}	13×10^{-8}	0.70	0.983	1.4×10^{-7}
	80	3.0×10^{5}	7.7×10^{-11}	0.92	3.0×10^{3}	8×10^{-6}	0.80	0.993	1.2×10^{-6}
	100	1.9×10^{4}	5.0×10^{-11}	0.98	3.0×10^{2}	1.8×10^{-2}	0.01	0.997	1.9×10^{-5}
	120	2.1×10^{3}	7.2×10^{-11}	0.96	2.0×10^{2}	1.0×10^{-2}	0.10	0.998	1.6×10^{-4}
	140	4.5×10^{2}	1.1×10^{-9}	0.83	2.0×10^{2}	1.5×10^{-2}	0.18	0.990	5.7×10^{-4}
	160	1.7×10^{2}	2.0×10^{-9}	0.80	1.2×10^{2}	4.0×10^{-2}	0.20	0.550	1.3×10^{-3}
	180	8.7×10^{1}	3.0×10^{-9}	0.80	2.5×10^{1}	9.0×10^{-2}	0.24	0.507	3.3×10^{-3}
	200	4.3×10^{1}	5.0×10^{-9}	0.80	2.0×10^{0}	2.0×10^{-1}	0.30	0.862	8.2×10^{-3}
$MAPbBr_3$	20	4.0×10^{7}	1.8×10^{-10}	0.78	5.3×10^{8}	8.8×10^{-9}	0.71	1.000	1.7×10^{-9}
	40	2.0×10^{6}	1.7×10^{-10}	0.78	3.5×10^{8}	3.3×10^{-8}	0.41	0.994	1.7×10^{-9}
	60	1.2×10^{7}	1.5×10^{-10}	0.77	1.0×10^{8}	1.2×10^{-7}	0.42	0.986	8.2×10^{-9}
	80	6.1×10^{6}	1.3×10^{-10}	0.80	2.1×10^{7}	4.3×10^{-7}	0.45	0.989	4.5×10^{-8}
	100	2.9×10^{6}	1.1×10^{-10}	0.83	1.0×10^{7}	4.0×10^{-6}	0.35	0.990	4.7×10^{-7}
	120	1.4×10^{5}	1.0×10^{-10}	0.88	1.0×10^{6}	2.0×10^{-5}	0.30	0.999	1.3×10^{-6}
	140	6.5×10^{5}	7.0×10^{-11}	0.91	2.1×10^{5}	6.0×10^{-5}	0.27	1.000	3.1×10^{-6}
	160	3.1×10^{5}	4.8×10^{-11}	0.95	6.0×10^{4}	3.0×10^{-4}	0.25	1.000	5.5×10^{-6}
	180	1.4×10^{5}	2.3×10^{-11}	0.95	1.0×10^{4}	2.0×10^{-3}	0.20	0.899	1.4×10^{-5}
	200	3.6×10^{4}	1.2×10^{-10}	0.91	1.0×10^{3}	1.0×10^{-2}	0.22	0.993	3.8×10^{-5}
$MAPbCl_3$	20	8.7×10^{6}	3.1×10^{-10}	0.81	5.1×10^{8}	1.1×10^{-8}	0.80	0.999	1.4×10^{-10}
	40	6.8×10^{6}	3.7×10^{-10}	0.79	5.1×10^{8}	1.2×10^{-8}	0.85	1.000	1.4×10^{-10}
	60	3.9×10^{6}	5.0×10^{-10}	0.78	1.0×10^{8}	2.6×10^{-8}	0.79	0.989	6.9×10^{-10}
	80	2.0×10^{6}	5.0×10^{-10}	0.81	1.7×10^{7}	15×10^{-8}	0.56	0.908	3.8×10^{-9}
	100	1.0×10^{6}	6.0×10^{-10}	0.76	8.0×10^{5}	23×10^{-7}	0.52	0.999	3.9×10^{-8}
	120	4.4×10^{5}	3.1×10^{-10}	0.83	2.0×10^{5}	15×10^{-6}	0.49	0.999	1.1×10^{-7}
	140	2.0×10^{5}	2.0×10^{-10}	0.87	8.0×10^{4}	33×10^{-6}	0.51	1.000	2.6×10^{-7}
	160	7.6×10^{4}	2.0×10^{-10}	0.91	8.0×10^{4}	15×10^{-5}	0.46	0.982	4.6×10^{-7}
	180	3.2×10^{4}	2.1×10^{-10}	0.91	2.8×10^{4}	16×10^{-5}	0.58	0.979	1.2×10^{-6}
	200	1.2×10^{4}	1.1×10^{-10}	0.94	1.0×10^{4}	27×10^{-5}	0.67	0.998	3.2×10^{-6}

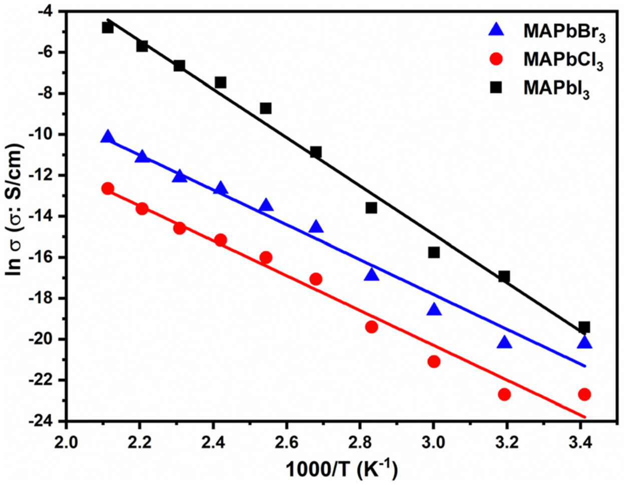

Fig. 6 Temperature dependence of the conductivity of perovskites. $MAPbI_3$ (■), $MAPbBr_3$ (▲) and $MAPbCl_3$ (●), respectively. Symbols mean experimental results obtained from the Nyquist plot and the lines mean the Arrhenius fit.

temperatures studied. Such behavior has been necessary to understand the dynamics process of the different agents of perovskites. However, a little change can be observed around 100 °C in the conductivity patterns of all samples indicating that the perovskites exhibit significant similarities, being more prominent for $MAPbBr_3$ and $MAPbCl_3$. In both cases an increase in conductivity as temperature rises is evident.

From Fig. 6 we have calculated the activation energy associated with the conductivity. For this we have fitted the experimental results of the conductivities obtained from the Nyquist plot shown in Fig. 5 for all perovskites. The values of the activation energy follow the trend E_{act} ($MAPbBr_3$) = (70.7 ± 4.0) kJ mol^{-1} (*i.e.*, 0.73 ± 0.04 eV) < E_{act} ($MAPbCl_3$) = (71.5 ± 4.0) kJ mol^{-1} (*i.e.*, 0.74 ± 0.04 eV) < E_{act} ($MAPbI_3$) = (98.1 ± 3.6) kJ mol^{-1} (*i.e.*, 1.02 ± 0.04 eV).

It is noteworthy that the conductivity of the $MAPbBr_3$ sample is slightly higher than that of the $MAPbCl_3$ sample. However, upon analyzing the $MAPbI_3$ sample a remarkably mild alteration in conductivity becomes evident at temperatures between 80 °C and 100 °C. This sudden change might be attributed to the structural modifications that occur as the temperature surpasses these values, which might be due to a change in wettability and a change in the crystallinity and size of crystal grains. It is likely that the properties of the material undergo significant shifts due to these temperature thresholds. Notice that these sudden changes in behavior have also been observed at temperatures higher than 100 °C from XRD for $MAPbI_3$, indicating that PbI_2 is not fully converted to perovskite and an increase in the temperature results in the degradation of the $MAPbI_3$ phase.[56]

Considering the nature of these materials, it is noteworthy that at temperatures exceeding 80–100 °C, distinct relaxation or orientation processes can be induced in both the inorganic and organic ions present within the samples. It is intriguing to observe that these processes tend to manifest more gradually in the case of $MAPbI_3$, as opposed to perovskites with Cl or Br. This phenomenon aligns with findings described by various researchers,[57–59] who suggest a connection between these behaviors and the reorientation angle of MA^+ ions. These observations could be attributed to the constraints imposed by the stacking of the PbI64 octahedral framework in a TP (tetrahedral) arrangement. This arrangement might impact the intramolecular or axial rotation of organic cations along with intricate hydrogen bonding interactions with inorganic cages. These factors could collectively contribute to the observed variations in relaxation and orientation processes within the distinct types of perovskite materials.[57–61]

In $MAPbI_3$, the presence of iodide vacancies allows for the migration of iodide, and thus iodide vacancies also migrate.[11,12] The latter are formed, for example, when an iodide ion at a regular lattice site moves to an interstitial site, leaving an iodide vacancy at the original iodide lattice site (referred to as the (anion) Frenkel defect).[13] Alternatively. the formation of Schottky defects, which results in the formation of MA vacancies and iodide vacancies, is well possible in $MAPbI_3$ and results in the formation of iodide vacancies,[12,14] Iodide interstitials, iodide or MA vacancies, all represent classical point defects that can widely determine the electrical transport behavior of halide perovskites.[5] Accordingly, defect chemical modeling combined with appropriate characterization methods offers a powerful way to gain in-depth understanding of the electrical conductivity in halide perovskites.[13,15,16]

From Fig. 6 we have calculated the activation energy associated with the conductivity. For this we have fitted the experimental results of the conductivities obtained from the Nyquist plot shown in Fig. 5 for all perovskites. The values of the activation energy follow the trend E_{act} ($MAPbBr_3$) = (70.7 ± 4.0) kJ mol^{-1} (*i.e.*, 0.73 ± 0.04 eV) < E_{act} ($MAPbCl_3$) = (71.5 ± 4.0) kJ mol^{-1} (*i.e.*, 0.74 ± 0.04 eV) < E_{act} ($MAPbI_3$) = (98.1 ± 3.6) kJ mol^{-1} (*i.e.*, 1.02 ± 0.04 eV).

Fig. 7 presents the frequency dependencies of the real and imaginary parts of the complex modulus for the sample $MAPbCl_3$. The corresponding behaviors for the other perovskites, $MAPbI_3$ and $MAPbBr_3$, can be found in the ESI† (Fig. SI5 and SI6). Examining Fig. 7, we can observe that the variations of the real part of the complex modulus (M') tend to converge towards zero at lower frequencies, while at higher frequencies, they tend towards $1/\varepsilon_{r.\infty}$, where $\varepsilon_{r.\infty}$ denotes the electrical permittivity of the perovskite. The values determined in our study were 30 ± 2, 29 ± 2 and 31 ± 1 for $MAPbCl_3$, $MAPbBr_3$ and $MAPbI_3$, respectively. These values are quite similar to the value 30, considered by Prochowicz *et al.*[62] to calculate the defect density in the perovskite $MAPbI_3$.

In contrast, the complex modulus M'' displays frequency-dependent changes, characterized by a symmetrical peak with varying width that decreases with rising temperature in the case of the $MAPbCl_3$ sample. This symmetry is also present for the $MAPbBr_3$ sample. However, for the $MAPbI_3$ sample, the behavior is notably asymmetric, with two peaks observed at lower temperatures. This asymmetry might be attributed to the sample's tendency to retain moisture, influencing the mobility of two distinct ions, I^- and H^+. The frequency at the point of maximum is intricately connected to the relaxation time (τ_M). This reciprocal relationship can be elucidated by considering the values derived for $\omega_M = 2\pi f_M$ from the peaks identified for M''. Notably, these values correspond to the relaxation time and, by extension, will be contingent on the prevailing temperature conditions.

As depicted in Fig. 8, the relationship between relaxation time and temperature is non-linear. On one hand, both $MAPbCl_3$ and $MAPbBr_3$ samples demonstrate a similar trend across the entire temperature range, featuring two distinct thermally activated processes. On the other hand, the $MAPbI_3$ sample exhibits two distinct behaviors: one below 120 °C

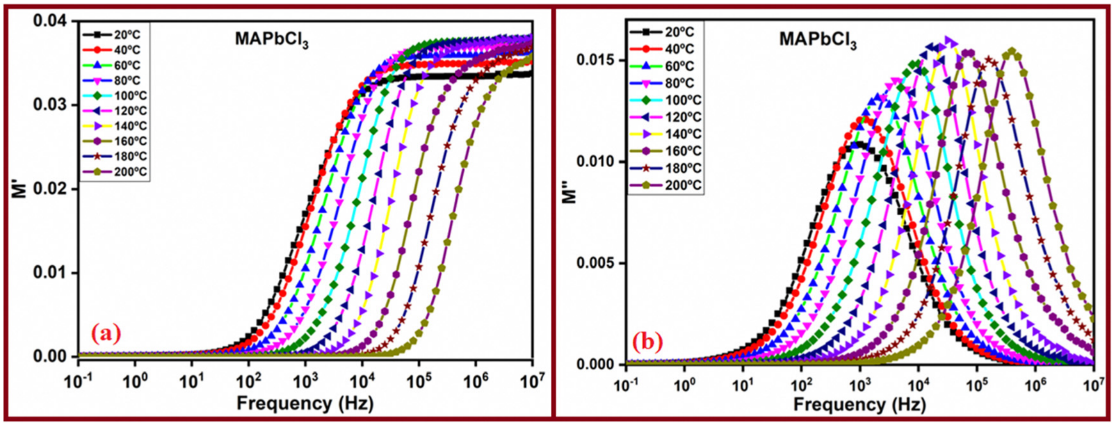

Fig. 7 The frequency-dependent behaviors of the (a) real part and (b) imaginary part of the dielectric complex modulus for the perovskite $MAPbCl_3$ over a temperature range spanning from 20 °C to 200 °C, with intervals of 20 °C.

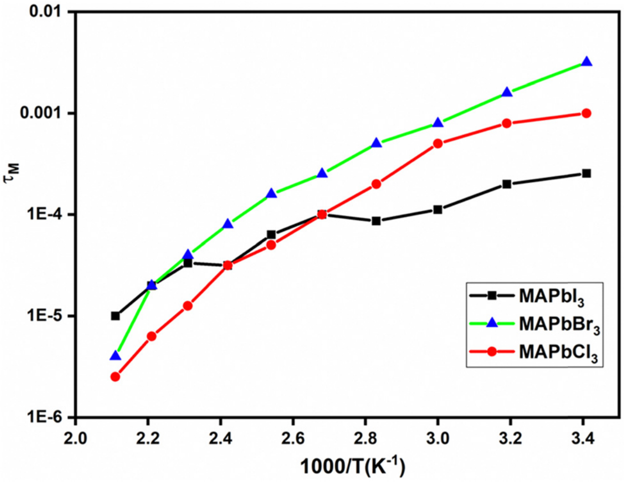

Fig. 8 Arrhenius plot of the relaxation time obtained from the peaks of the complex modulus, M'', for the perovskites, observed over the temperature range from 20 °C to 200 °C.

and another above this temperature. This behavior presents variations that could potentially be linked to the effects of degradation leading to abrupt structural changes or could be related to changes in iodine vacancies and holes between low and high temperatures, as observed for the total conductivity of the $MAPbI_3$ perovskite as a function of the iodine partial pressure.[55] These structural changes are likely to involve intramolecular or axial rotations of organic cations, coupled with subtle hydrogen bond interactions with inorganic cages. Such changes are particularly relevant in the context of our perovskites containing I^-, Cl^-, and Br^- ions.[58–62] Remarkably, these behaviors stand in contrast to the alterations observed in conductivity. This can be attributed to the consistent value of the real part of permittivity at frequencies approaching infinity, as demonstrated in Fig. 7. It is important to consider that $\tau = \varepsilon_{r.\infty}/\sigma$, reinforcing the reciprocal relationship between relaxation time and conductivity alterations.

3.4.3. Mobility, diffusivity, Debye length and charge carrier density. Mobility and diffusion coefficient are vital parameters for characterizing a material when subjected to an electric field.[22–34] In cases where a simple Debye relaxation effectively describes the dielectric behavior of the loss tangent ($\tan\delta$) of a sample, a distinct peak is observed. This is notably evident in the Nyquist plot, where a semicircle emerges, and the point of intersection between the real and imaginary parts of impedance, where the imaginary part is zero, determines the sample's resistance. This behavior can be attributed to the fact that the impedance spectrum of perovskites is essentially dictated by the movement of a single type of ion, resulting in the observation of a sole relaxation time. By identifying the maxima in $\tan\delta$ values, it is possible to estimate the diffusion coefficient of the charges in the perovskites[25,59,63]

$$D = \frac{\omega_{\max}^{\tan\delta} \cdot L^2}{32(\tan^3\delta)_{\max,\omega}} \tag{8}$$

and from the values obtained for the diffusion coefficient D, the mobility (μ) can be obtained from the Einstein relation as

$$\mu = \frac{qD}{k_B T} \tag{9}$$

where k_B is the Boltzmann constant, T stands for the temperature, and q is the charge of a monovalent cation.

Fig. 9 presents the experimental $\tan\delta$ values for the perovskites across all temperatures. Moreover, a noteworthy observation can be rationalized: the displacement of the loss tangent peaks towards the higher frequency side is closely linked to the activation of anions I^-, Cl^-, and Br^-. On the other hand, the value of the loss tangent of the peak is higher in the case of $MAPbBr_3$ and $MAPbCl_3$ than that in the case of $MAPbI_3$, and a change in this intensity is clearly observed between low and high temperatures for all the perovskites. This behavior mirrors the findings observed for electrolytes incorporating ionic liquids.[64–67] Based on the peaks observed in these figures, we have extracted the values of $\omega_{\max}^{\tan\delta}$ and $(\tan^3\delta)_{\max.\omega}$. With knowledge of the samples' thickness, we calculated the diffusion coefficients of the perovskites, and utilizing eqn (8), we then computed the corresponding mobilities. This series of calculations provides valuable insights into the mobility of charged particles within these materials under specific conditions.

Fig. 10 illustrates the temperature-dependent diffusion and mobility coefficients of the perovskites. From Fig. 10A, it becomes apparent that the diffusion coefficient values decline as the temperature rises. This behavior stands in stark contrast to what is typically observed in ionic diffusion through polymer electrolytes.[34,65,66] Upon a thorough examination of this figure, a remarkable trend emerges: the diffusion coefficients exhibit impressive performance at lower temperatures, subsequently declining by approximately three orders of magnitude when comparing the diffusivity at 40 °C to that at 120 °C. On a contrasting note, across the entire temperature range, two distinct variations become evident, similar to the variations observed in the temperature-dependent behavior of conductivity. This behavior is expected and can be attributed to the similar patterns exhibited by the mobilities of perovskites.

On the other hand, a close inspection of Fig. 10b shows that the mobilities of perovskites follow the trend $\mu(MAPbI_3) > \mu(MAPbCl_3) > \mu(MAPbBr_3)$. In the case of the $MAPbI_3$ perovskite we have found that mobility varies between 6×10^{-10} m^2 V^{-1} s^{-1} and 4×10^{-6} m^2 V^{-1} s^{-1}, depending on temperature. These values for $MAPbBr_3$ and $MAPbCl_3$ are slightly lower than the corresponding electronic mobilities found in the literature (4×10^{-5}–35×10^{-4} m^2 V^{-1} s^{-1}).[67] However, in the case of $MAPbI_3$ they are quite similar. For example, at 80 °C the value found in this work was 7×10^{-7} m^2 V^{-1} s^{-1} (*i.e.*, 7×10^{-3} cm^2 V^{-1} s^{-1} found by Stranks *et al.*[68]). On the other hand, our values for all perovskites are higher than the values given by ref. 55 and 68, where the values found at 70 °C for $MAPbI_3$ were significantly lower ($\mu_{Vi^*} \cong 5 \times 10^{-8}$ cm^2 V^{-1} s^{-1} and $\mu_{MA} \cong 8 \times 10^{-11}$ cm^2 V^{-1} s^{-1}), respectively.

In general, in polyelectrolytes and semiconductors considered as binary systems, the total electrical conductivity is the

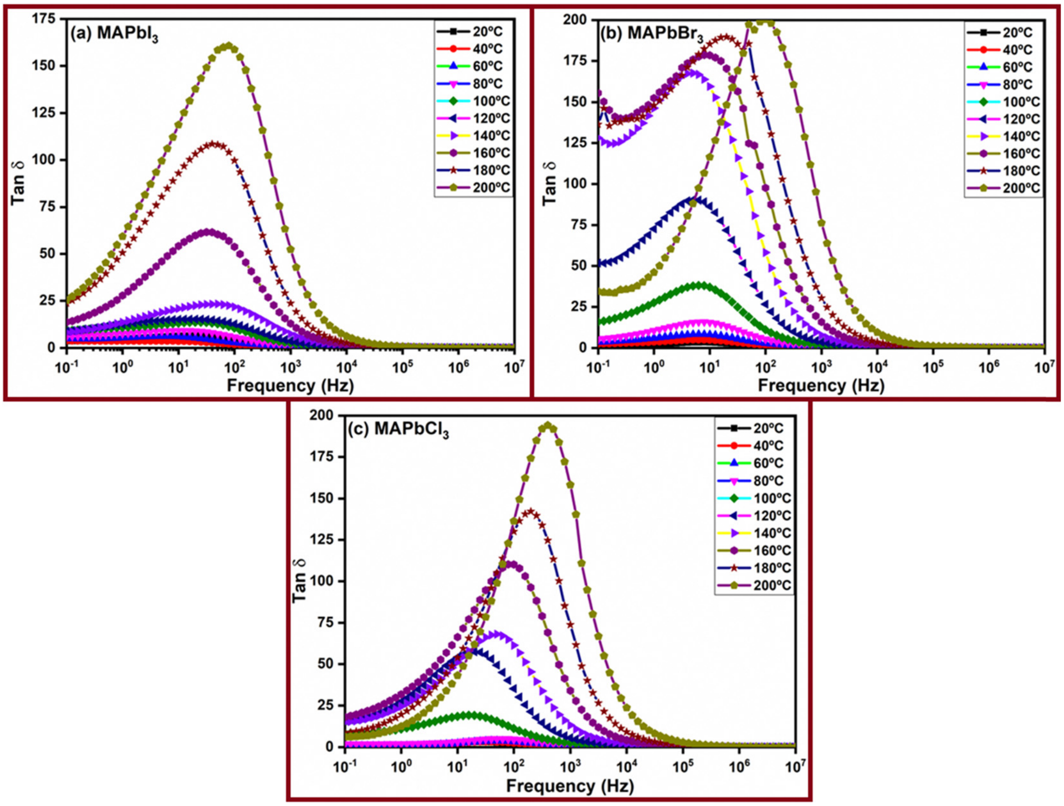

Fig. 9 The variation of loss tan δ with frequency for perovskites: (a) MApbI$_3$, (b) MAPbBr$_3$, and (c) MAPbCl$_3$, in the entire range of temperatures studied.

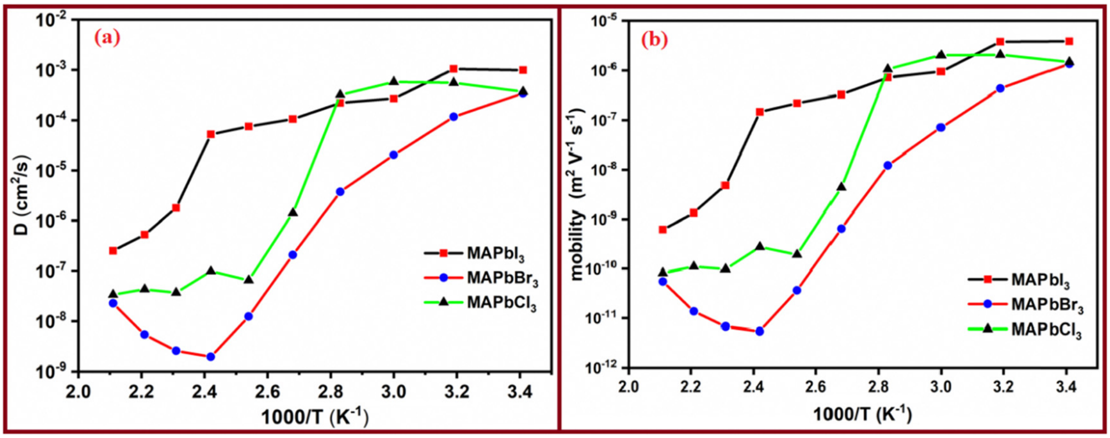

Fig. 10 The temperature-dependent behaviors of (a) diffusivity and (b) mobility of the perovskites.

sum of the contributions of all the constituent charge carriers, *i.e.*, $\sigma = \sigma^+ + \sigma^-$. In the case of perovskites MAPbX$_3$ (X = Cl, Br, I) the highest possible contribution to the ionic conductivity is from the anions. Therefore, the anion conductivity can be estimated supposing that the anion transference number is practically equal to one. In this approximation, the cations are practically immobile due to the reduced mobility because their size in comparison with the other counterpart is higher. Therefore, the cation mobility is negligible and thus the dominated mobility will be mainly restricted to the anion contribution (*i.e.*, X$^-$ = Cl$^-$, Br$^-$ and I$^-$, respectively). In these cases, the ionic conductivity can be described as $\sigma^- = \sigma$. If charge carriers do not interact with each other, we can estimate the charge carrier density, (n), from the Nernst–Einstein relationship and eqn (9) as

$$n = \frac{\sigma k_B T}{q^2 D} \tag{10}$$

The charge carrier density of the perovskites in the entire range of temperatures studied is given in Fig. 11.

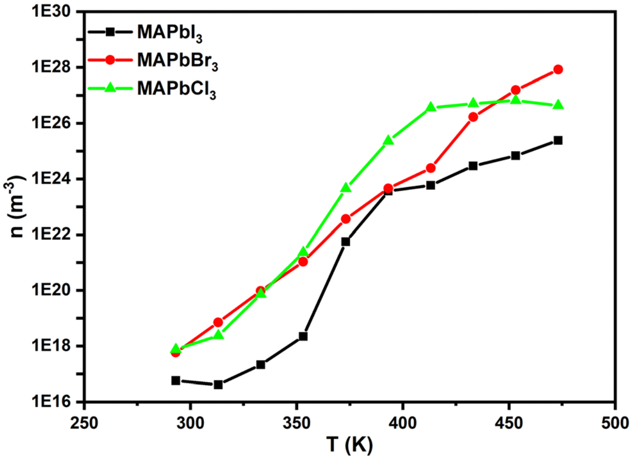

Fig. 11 The variation of the charge carrier density (n) with the temperature for the perovskites.

From Fig. 11 we can see that in the perovskites the charge carrier's density, n (m^{-3}), increases with the temperature increase, with its value being around 10^{17} m^{-3} at 20 °C and 10^{27} m^{-3} at 180 °C for the perovskites MAPbCl$_3$ and MAPbBr$_3$. For both perovskites, in the entire range of temperatures studied the charge carrier's density is the highest compared to that of MAPBI$_3$. This is due to the fact that the relation σ/D is lower for MAPbI$_3$ than that for the others. On the other hand, a change of behavior at 100 °C seems to be observed. Finally, these values agree with the range of literature-based values calculated, as observed for MAPbI$_3$.[69]

Lastly, to understand the interface effects between MAPbI$_3$ and reference MAPbCl$_3$, we have calculated the Debye length based on the peaks of loss tangent ($\tan\delta$) following ref. 23, 25, 34 and 63. It is important to note that there is an error in eqn (23) of ref. 63. The accurate expression should be:

$$L_D^{-1} = \frac{8(\tan\delta_{\max})^2}{L} \tag{11}$$

A rigorous deduction of eqn (11) is given in ref. 24 and 70. This has been described recently in the ESI† of ref. 24. Notice that the Debye length can be determined using eqn (11) because in our perovskites the relaxation time for redistribution of ions is large satisfying the condition that $\frac{L}{L_D} \gg 1$. It is interesting to note that the determination of the Debye length, defined as $L_D = \sqrt{\frac{\varepsilon_\infty \cdot \varepsilon_0 \cdot k_B \cdot T}{n \cdot q^2}}$, where k_B is the Boltzmann constant, T the temperature, ε_0 the vacuum permittivity, ε_∞ the static permittivity, q the charge quantity of the ion and n the ionic charge density imbibed into the perovskites, has been carried out without the need to know the values of ε_∞ and the density of the charge carriers (n), which must be determined by means of knowledge of mobility (μ) or diffusivity (D). This avoids the possible errors that the models provide in the determination of these parameters. In our case, we have opted for its determination based on the experimental results of the loss tangent for each of the perovskites where the curves of loss tangent display peaks corresponding to the maxima in $\tan\delta$, which are associated with the conductivity. In this way, the value of L_D is calculated from the experimental results obtained for $\tan\delta$ from EIS and therefore we think that it will have less error than if it had been determined from the values of the parameters such as n, D, τ, or μ, where models are necessary for its determination.

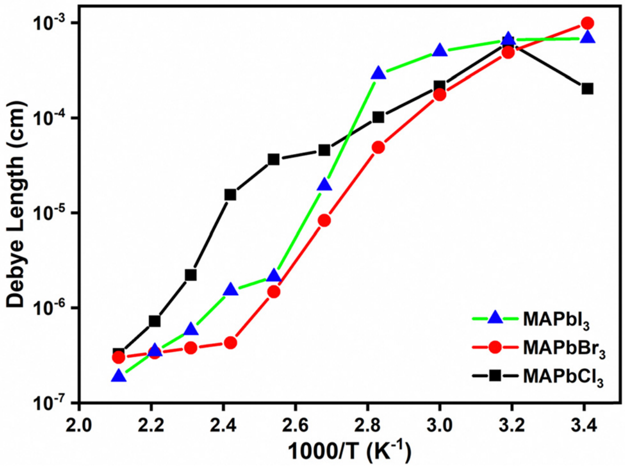

Fig. 12 The values of the Debye length that were computed using eqn (11) for the perovskites examined across the entire range of temperatures studied.

By utilizing eqn (11) and leveraging the experimental values acquired for $\tan\delta_{\max}$ for the various perovskites, we derived the Debye length values. These results have been graphed in Fig. 12, providing a visual representation of the Debye lengths corresponding to the different perovskites.

As shown in Fig. 12, the calculated results for the Debye length, obtained from the peaks of the loss tangent using eqn (11), exhibit a similar behavior for the perovskites MAPbCl$_3$ and MAPbBr$_3$ throughout the entire range of temperatures studied. In contrast, the perovskite MAPbI$_3$ displays an abnormal behavior, with a drastic decrease in the thickness of the Debye layer observed from 50 °C onwards. These distinct behaviors may be related to the long or short-range hopping distances that the anions have to overcome to move and transfer electrons to the conduction band. The difference in the behavior of MAPbI$_3$ could indicate the unique charge transport characteristics of this particular perovskite, which may be influenced by the type of anions and their mobility at different temperatures. Our results for MAPbI$_3$ were $L_D \cong 2 \times 10^{-6}$ m, at 20 °C, agreeing with the values observed by Samuel D. Stranks *et al.*[71] where Debye lengths of 120 nm and 105 nm for electron and holes were obtained in the case of MAPbI$_3$. Further investigation is needed to fully understand the underlying mechanisms behind these observed trends.

4. Conclusions

Various perovskite powders of MAPbX$_3$ were synthesized, where X represents iodine (I), bromine (Br), or chlorine (Cl). The main objective of this research was to investigate the influence of different halides on the photovoltaic performance of perovskites. To achieve this, several characterization methods were conducted to understand the properties of the perovskite powders $MAPbX_3$ (X = I, Br, Cl) with a specific focus on determining their optical and conductivity properties. The corresponding X-ray diffraction (XRD) spectrum of each perovskite powder sample is also shown in Fig. 1. The XRD spectra displayed characteristic peaks that aligned well with those reported in the literature. This indicates that the prepared perovskite powders have a well-defined crystalline structure consistent with the known properties of $MAPbX_3$ compounds. Overall, the HRTEM analysis provided valuable insights into the nanostructure, crystal quality, and crystallographic information of the $MAPbX_3$ perovskite powders. These findings are essential for a comprehensive understanding of the properties and potential applications of these perovskite materials. This study contributes to the advancement of knowledge in the field of perovskite materials and their use in various applications.

The UV-visible spectra of perovskite powders ($MAPbCl_3$, $MAPbBr_3$, and $MAPbI_3$) were analyzed, revealing distinct absorption onsets for each composition, with $MAPbCl_3$ absorbing light in the ultraviolet and visible regions at 427 nm, $MAPbBr_3$ absorbing at 563 nm in the visible spectrum, and $MAPbI_3$ absorbing at 843 nm in the near-infrared region. The corresponding optical bandgap values are 2.90 eV, 2.20 eV, and 1.47 eV, respectively.

The analysis of electrochemical impedance spectroscopy reveals that perovskite materials with iodine (I), chlorine (Cl), and bromine (Br) exhibit optimal conductivities, making them suitable semiconductor materials. As the temperature increases, their conductivities also increase, following the trend σ_{dc} ($MAPbI_3$) $<$ σ_{dc} ($MAPbCl_3$) $<$ σ_{dc} ($MAPbBr_3$). Furthermore, the conductivity activation energies of these materials vary with temperature. The values of the activation energy follow the trend E_{act} ($MAPbBr_3$) = (70.7 ± 4.0) kJ mol^{-1} (*i.e.*, 0.73 ± 0.04 eV) $<$ E_{act} ($MAPbCl_3$) = (71.5 ± 4.0) kJ mol^{-1} (*i.e.*, 0.74 ± 0.04 eV) $<$ E_{act} ($MAPbI_3$) = (98.1 ± 3.6) kJ mol^{-1} (*i.e.*, 1.02 ± 0.04 eV).

Electrochemical impedance spectroscopy (EIS) studies revealed a significant change in the conductivity of the $MAPbI_3$ perovskite at temperatures between 80 °C and 120 °C. This change could be attributed to structural modifications induced when the temperature exceeds these values. The through-plane conductivity increases around 10^3 times when the temperature increases from 60 °C to 120 °C and around 100 times from 120 °C to 200 °C. Meanwhile, the sheet conductivity (in-plane conductivity) measured at ambient temperature reveals that sheet resistivity obtained for the perovskites expressed in terms of the International Annealed Copper Standard (% IACS) is about 0.1% IACS, a value equivalent to 1000 times lower than annealed copper. The sheet conductivities were 489×10^3 S m^{-1}, 486×10^3 S m^{-1} and 510×10^3 S m^{-1} for $MAPbBr_3$, $MAPbCl_3$ and $MAPbI_3$, respectively.

At low temperatures, the diffusivities of the perovskite materials exhibit a significant decrease of approximately three orders of magnitude when comparing the diffusivity values at 40 °C to those at 120 °C. Moreover, throughout the entire range of temperatures studied, two distinct variations in diffusivity are observed, which resemble the behavior observed in the variation of conductivity with temperature. Similarly, perovskite mobility also displays a similar behavior. In the case of the $MAPbI_3$ perovskite we have found that mobility varies between 6×10^{-10} m^2 V^{-1} s^{-1} and 4×10^{-6} m^2 V^{-1} s^{-1}, depending on temperature. These values for $MAPbBr_3$ and $MAPbCl_3$ are slightly lower than the corresponding electronic mobility found in the literature (4×10^{-5}–35×10^{-4} m^2 V^{-1} s^{-1}). The variation of relaxation time with temperature is not linear. The samples $MAPbCl_3$ and $MAPbBr_3$ show a similar tendency over the entire temperature range studied, with two different thermally activated processes. However, the sample $MAPbI_3$ exhibits two distinct behaviors, one below 120 °C and the other above this temperature, with a variation that could potentially be associated with possible degradation effects leading to sudden structural changes.

This study provides valuable insights for optimizing the performance of perovskite solar cells. Understanding how dopants influence the electrical conductivity and photovoltaic properties of the perovskite materials, this work will enable researchers to design and engineer more efficient and stable solar cell devices based on $MAPbX_3$ perovskites. These findings indicate that the conductivity of the perovskite materials is temperature-dependent, and the variations can significantly impact their performance as semiconductor materials at different temperatures.

Author contributions

Shafi Ullah: conceptualization, investigation, methodology, writing – original draft; Andreu Andrio: investigation, supervision, validation; Julia Marí-Guaita: conceptualization, investigation, methodology, writing – original draft; Hanif Ullah: investigation, methodology; writing – original draft; Antonio Méndez-Blas: visualization, reviewing, visualization, reviewing and editing; Bernabe Mari: visualization, supervision, validation; Roxana M. del Castillo Vázquez: visualization, reviewing, visualization, reviewing and editing; and Vicente Compañ: conceptualization, investigation, methodology, writing – original draft, visualization supervision, validation, reviewing, and editing.

Conflicts of interest

The authors declare that they have no known competing financial interests or personal relationships that could have appeared to influence the work reported in this paper.

Acknowledgements

The author Shafi Ullah acknowledges the post-doctoral contract supported by the RRHH (Human Resources for Research) program, postdoctoral contract (PAID-10-20) Universitat Politècnica de Valencia (UPV), and Ministerio de Economía y

Competitividad under Grant Number PID 2019–107137 RB-C21. Antonio Mendez-Blas acknowledges CONACYT, Mexico (Sabbatical Grant 2022) and VIEP-BUAP.

References

1 J. Burschka, N. Pellet, S. J. Moon, R. Humphry-Baker, P. Gao, M. K. Nazeeruddin and M. Grätzel, Sequential deposition as a route to high-performance perovskite-sensitized solar cells, *Nature*, 2013, **499**(7458), 316–319.

2 H. S. Kim, C. R. Lee, J. H. Im, K. B. Lee, T. Moehl, A. Marchioro and S. J. Moon, *et al.*, Lead iodide perovskite sensitized all-solid-state submicron thin film mesoscopic solar cell with efficiency exceeding 9%, *Sci. Rep.*, 2012, **2**(1), 591.

3 J. H. Im, C. R. Lee, J. W. Lee, S. W. Park and N. G. Park, 6.5% efficient perovskite quantum-dot-sensitized solar cell, *Nanoscale*, 2011, **3**(10), 4088–4093.

4 P. V. Nrel, *Research cell record efficiency chart*, 2018.

5 H. Tsai, W. Nie, J. C. Blancon, C. C. Stoumpos, R. Asadpour, B. Harutyunyan and A. J. Neukirch, *et al.*, High-efficiency two-dimensional Ruddlesden–Popper perovskite solar cells, *Nature*, 2016, **536**(7616), 312–316.

6 J. A. Christians, P. Schulz, J. S. Tinkham, T. H. Schloemer, S. P. Harvey, B. J. Tremolet de Villers, A. Sellinger, J. J. Berry and J. M. Luther, Tailored interfaces of unencapsulated perovskite solar cells for >1000 hour operational stability, *Nat. Energy*, 2018, **3**(1), 68–74.

7 M. Saliba, J. P. Correa-Baena, C. M. Wolff, M. Stolterfoht, N. Phung, S. Albrecht, D. Neher and A. Abate, How to Make over 20% Efficient Perovskite Solar Cells in Regular (n–i–p) and Inverted (p–i–n) Architectures, *Chem. Mater.*, 2018, **30**(13), 4193–4201.

8 D. Prochowicz, P. Yadav, M. Saliba, M. Saski, S. M. Zakeeruddin, J. Lewinski and M. Gratzel, Reduction in the interfacial trap density of mechanochemically synthesized $MAPbI_3$, *ACS Appl. Mater. Interfaces*, 2017, **9**(34), 28418–28425.

9 C. Das, A. K. Singh, Y. Heo, G. Aggarwal, S. K. Maurya, J. Seidel and B. Kavaipatti, Effect of grain boundary cross-section on the performance of electrodeposited Cu_2O photocathodes, *J. Phys. Chem. C*, 2018, **122**(3), 1466–1476.

10 A. Waleed, M. M. Tavakoli, L. Gu, Z. Wang, D. Zhang, A. Manikandan, Q. Zhang, R. Zhang, Y. L. Chueh and Z. Fan, Lead-free perovskite nanowire array photodetectors with drastically improved stability in nanoengineering templates, *Nano Lett.*, 2017, **17**(1), 523–530.

11 H. D. Kim, N. Yanagawa, A. Shimazaki, M. Endo, A. Wakamiya, H. Ohkita, H. Benten and S. Ito, Origin of open-circuit voltage loss in polymer solar cells and perovskite solar cells, *ACS Appl. Mater. Interfaces*, 2017, **9**(23), 19988–19997.

12 D. Prochowicz, P. Yadav, M. Saliba, M. Saski, S. M. Zakeeruddin, J. Lewiński and M. Grätzel, Mechanosynthesis of pure phase mixed-cation $MA_xFA_{1-x}PbI_3$ hybrid perovskites: photovoltaic performance and electrochemical properties, *Sustainable Energy Fuels*, 2017, **1**(4), 689–693.

13 A. Karmakar, A. M. Askar, G. M. Bernard, V. V. Terskikh, M. Ha, S. Patel, K. Shankar and V. K. Michaelis, Mechanochemical synthesis of methylammonium lead mixed–halide perovskites: unraveling the solid-solution behavior using solid-state NMR, *Chem. Mater.*, 2018, **30**(7), 2309–2321.

14 M. Saski, D. Prochowicz, W. Marynowski and J. Lewiński, Mechanosynthesis, Optical, and Morphological Properties of MA, FA, Cs-SnX_3 (X = I, Br) and Phase-Pure Mixed-Halide $MASnI_xBr_{3-x}$ Perovskites, *Eur. J. Inorg. Chem.*, 2019, (22), 2680–2684.

15 Z. Hong, D. Tan, R. A. John, Y. K. E. Tay, Y. K. T. Ho, X. Zhao, T. C. Sum, N. Mathews, F. García and H. S. Soo, Completely solvent-free protocols to access phase-pure, metastable metal halide perovskites and functional photodetectors from the precursor salts, *iScience*, 2019, **16**, 312–325.

16 B. Dou, L. M. Wheeler, J. A. Christians, D. T. Moore, S. P. Harvey, J. J. Berry, F. S. Barnes, S. E. Shaheen and M. F. van Hest, Degradation of highly alloyed metal halide perovskite precursor inks: mechanism and storage solutions, *ACS Energy Lett.*, 2018, **3**(4), 979–985.

17 D. Prochowicz, P. Yadav, M. Saliba, D. J. Kubicki, M. M. Tavakoli, S. M. Zakeeruddin, J. Lewiński, L. Emsley and M. Grätzel, One-step mechanochemical incorporation of an insoluble cesium additive for high performance planar heterojunction solar cells, *Nano Energy*, 2018, **49**, 523–528.

18 S. Biberger, N. Leupold, C. Witt, C. Greve, P. Markus, P. Ramming and D. Lukas, *et al.*, First of their kind: Solar cells with a dry-processed perovskite absorber layer via powder aerosol deposition and hot-pressing, *Solar RRL*, 2023, **7**(16), 2300261.

19 M. Ouafi, L. Atourki, D. Barrit, R. F. Allah, H. Ouaddari and A. Ihlal, Structural and optical characterization of $CH_3NH_3PbX_3$ (X= I, Br and Cl) powder as precursor materials for perovskite based optoelectronic devices, *Mater. Chem. Phys.*, 2023, **301**, 127600.

20 B. Wang, X. Yang, S. Chen, S. Lu, S. Zhao, Q. Qian, W. Cai, S. Wang and Z. Zang, Flexible perovskite scintillators and detectors for X-ray detection, *iScience*, 2022, **25**(12), DOI: 10.1016/j.isci.2022.105593.

21 Z. Jia, J. Peng, L. Yu, T. Jiang, Y. Li, F. Yao, F. Ren and Q. Lin, Spray-coating of AgI incorporated metal halide perovskites for high-performance X-ray detection, *Chem. Eng. J.*, 2022, **450**, 138229.

22 V. Compañ, J. Escorihuela, J. Olvera, A. García-Bernabé and A. Andrio, Influence of the anion on diffusivity and mobility of ionic liquids composite polybenzimidazol membranes, *Electrochim. Acta*, 2020, **354**, 136666.

23 A. Andrio, S. I. Hernández, C. García-Alcántara, L. F. Del Castillo, V. Compañ and I. Santamaría-Holek, Temperature dependence of anomalous protonic and superprotonic transport properties in mixed salts based on CsH_2PO_4, *Phys. Chem. Chem. Phys.*, 2019, **21**(24), 12948–12960.

24 D. Nuevo, M. Cuesta, R. Porcar, A. Andrio, E. Garcia-Verdugo and V. Compañ, Novel electrolytes based on

mixtures of dimethyl sulfoxide task specific zwitterionic ionic liquid and lithium salts: synthesis and conductivity studies, *Chem. Phys.*, 2023, **575**, 112043.

25 T. S. Sørensen and V. Compañ, Complex permittivity of a conducting, dielectric layer containing arbitrary binary Nernst–Planck electrolytes with applications to polymer films and cellulose acetate membranes, *J. Chem. Soc., Faraday Trans.*, 1995, **91**(23), 4235–4250.

26 T. S. Sørensen, V. Compañ and R. Diaz-Calleja, Complex permittivity of a film of poly[4-(acryloxy) phenyl-(4-chlorophenyl) methanone] containing free ion impurities and the separation of the contributions from interfacial polarization, Maxwell–Wagner–Sillars effects and dielectric relaxations of the polymer chains, *J. Chem. Soc., Faraday Trans.*, 1996, **92**(11), 1947–1957.

27 J. R. Macdonald, Theory of ac space-charge polarization effects in photoconductors, semiconductors, and electrolytes, *Phys. Rev.*, 1953, **92**(1), 4.

28 J. R. MacDonald, Utility of Continuum Diffusion Models for Analyzing Mobile-Ion Immittance Data: Electrode, Bulk, and Generation–Recombination Effects, *J. Phys.: Condens. Matter*, 2010, **22**(49), 495101.

29 J. R. MacDonald, L. R. Evangelista, E. K. Lenzi and G. Barbero, Comparison of Impedance Spectroscopy Expressions and Responses of Alternate Anomalous Poisson-Nernst-Planck Diffusion Equations for Finite-Length Situations, *J. Phys. Chem. C*, 2011, **115**(15), 7648–7655.

30 H. J. Schütt, Determination of the Free Ionic Carrier Concentration: A Discussion of Different Methods, *Solid State Ionics*, 1994, 505–510.

31 H. J. Schütt and E. Gerdes, Space-Charge Relaxation in Ionicly Conducting Oxide Glasses. I. Model and Frequency Response, *J. Non-Cryst. Solids*, 1992, **144**, 1–13; R. Coelho, Sur La Relaxation d'une Charge d'espace, *Rev. Phys. Appl.*, 1983, **18**(3), 137–146.

32 R. Coelho, On the static permittivity of dipolar and conductive media—an educational approach, *J. Non-Cryst. Solids*, 1991, **131**, 1136–1139.

33 H. J. Schütt and E. Gerdes, Space-Charge Relaxation in Ionicly Conducting Glasses. II. Free Carrier Concentration and Mobility, *J. Non-Cryst. Solids*, 1992, **144**, 14–20.

34 R. J. Klein, S. Zhang, S. Dou, B. H. Jones, R. H. Colby and J. Runt, Modeling electrode polarization in dielectric spectroscopy: ion mobility and mobile ion concentration of single-ion polymer electrolytes, *J. Chem. Phys.*, 2006, **124**(14), DOI: 10.1063/1.2186638.

35 J. F. Blachot, O. Diat, J.-L. Putaux, A.-L. Rollet, L. Rubatat, C. Vallois, M. Müller and G. Gebel, Anisotropy of structure and transport properties in sulfonated polyimide membranes, *J. Membr. Sci.*, 2003, **214**, 31–42.

36 T. A. Zawodzinski, C. Derouin, S. Radzinski, R. J. Sherman, V. T. Smith, T. E. Springer and S. Gottesfeld, Water Uptake by and Transport Through Nafion® 117 Membranes, *J. Electrochem. Soc.*, 1993, **140**, 1041–1047.

37 J. Escorihuela, R. Narducci, V. Compañ and F. Costantino, Proton Conductivity of Composite Polyelectrolyte Membranes with Metal-Organic Frameworks for Fuel Cell Applications, *Adv. Mater. Interfaces*, 2019, **6**, 1801146.

38 J. Olvera-Mancilla, J. Escorihuela, L. Alexandrova, A. Andrio, A. García-Bernabé, L. F. Del Castillo and V. Compañ, Effect of metallacarborane salt H [COSANE] doping on the performance properties of polybenzimidazole membranes for high temperature PEMFCs, *Soft Matter.*, 2020, **16**(32), 7624–7635.

39 A. García-Bernabé, A. Rivera, A. Granados, S. V. Luis and V. Compañ, Ionic transport on composite polymers containing covalently attached and absorbed ionic liquid fragments, *Electrochim. Acta*, 2016, **213**, 887–897.

40 S. I. Hernández, B. Altava, J. A. Portillo-Rodríguez, I. Santamaría-Holek, C. García-Alcántara, S. V. Luis and V. Compañ, The Debye Length and Anionic Transport Properties of Composite Membranes Based on Supported Ionic Liquid-like Phases (SILLPS), *Phys. Chem. Chem. Phys.*, 2022, **24**(48), 29731–29746.

41 W. Feng, J. F. Liao, X. Chang, J. X. Zhong, M. Yang, T. Tian and Y. Tan, *et al.*, Perovskite crystals redissolution strategy for affordable, reproducible, efficient and stable perovskite photovoltaics, *Mater. Today*, 2021, **50**, 199–223.

42 J. Ding, H. Fang, Z. Lian, J. Li, Q. Lv, L. Wang, J. L. Sun and Q. Yan, A self-powered photodetector based on a $CH_3NH_3PbI_3$ single crystal with asymmetric electrodes, *CrystEngComm*, 2016, **18**(23), 4405–4411.

43 W. Wang, Z. Mai, Y. Chen, J. Wang, L. Li, Q. Su, X. Li and X. Hong, A label-free fiber optic SPR biosensor for specific detection of C-reactive protein, *Sci. Rep.*, 2017, **7**(1), 16904.

44 T. Baikie, N. S. Barrow, Y. Fang, P. J. Keenan, P. R. Slater, R. O. Piltz, M. Gutmann, S. G. Mhaisalkar and T. J. White, A combined single crystal neutron/X-ray diffraction and solid-state nuclear magnetic resonance study of the hybrid perovskites $CH_3NH_3PbX_3$ (X = I, Br and Cl), *J. Mater. Chem. A*, 2015, **3**(17), 9298–9307.

45 A. Poglitsch and D. Weber, Dynamic disorder in methyl ammonium trihalogenoplumbates(II) observed by millimeter-wave spectroscopy, *J. Chem. Phys.*, 1987, **87**(11), 6373–6378.

46 G. P. Nagabhushana, R. Shivaramaiah and A. Navrotsky, Direct calorimetric verification of thermodynamic instability of lead halide hybrid perovskites, *Proc. Natl. Acad. Sci. U. S. A.*, 2016, **113**(28), 7717–7721.

47 Y. Dang, Y. Liu, Y. Sun, D. Yuan, X. Liu, W. Lu, G. Liu, H. Xia and X. Tao, Bulk crystal growth of hybrid perovskite material $CH_3NH_3PbI_3$, *CrystEngComm*, 2015, **17**(3), 665–670.

48 S. Tang, X. Xiao, J. Hu, B. Gao, H. Chen, Z. Peng, J. Wen, M. Era and D. Zou, Solvent-Free Mechanochemical Synthesis of a Systematic Series of Pure-Phase Mixed-Halide Perovskites MAPb $(I_xBr_{1-x})_3$ and MAPb$(Br_xCl_{1-x})_3$ for Continuous Composition and Band-Gap Tuning, *ChemPlusChem*, 2020, **85**(1), 240–246.

49 A. Osherov, Y. Feldman, I. Kaplan-Ashiri, D. Cahen and G. Hodes, Halide diffusion in $MAPbX_3$: limits to topotaxy for halide exchange in perovskites, *Chem. Mater.*, 2020, **32**(10), 4223–4231.

50 A. Kanwat, E. Moyen, S. Cho and J. Jang, Rubidium as an alternative cation for efficient perovskite light-emitting diodes, *ACS Appl. Mater. Interfaces*, 2018, **10**(19), 16852–16860.

51 S. Saber, B. Marí, A. Andrio, J. Escorihuela, N. Khattab, A. Eid, A. E. Nahrawy, M. Abo Aly and V. Compañ, Structural and Electrochemical Analysis of CIGS: Cr Crystalline Nanopowders and Thin Films Deposited onto ITO Substrates, *Nanomaterials*, 2021, **11**(5), 1093.

52 H. Shi, F. Cao, T. Wang, H. Zhang, H. Gao, H. Liu, L. Gao, J. Zou, Y. Jiang and S. Liang, A well-balanced strength and electrical conductivity in rolled composite prepared by in-situ TiB2p/Cu composite powder, *J. Mater. Res. Technol.*, 2023, **27**, 1–10.

53 C. Dindault, H. Jun, D. Tondelier, B. Geffroy, J. E. Bourée, Y. Bonnassieux, P. Schulz and S. Swaraj, Metal halide perovskite layers studied by scanning transmission X-ray microscopy, *RSC Adv.*, 2022, **12**(39), 25570–25577.

54 D. Chicco, M. J. Warrens and G. Jurman, The coefficient of determoination R-squared is more informative than SMAPE,MAE, MAPE, MSE and RMSE in regression analysis evaluation, *Peer J. Comput. Sci.*, 2021, 1–24, DOI: 10.7717/peerj-cs.623.

55 N. Leupold, A. L. Seibel, R. Moos and F. Panzer, Electrical conductivity of halide perovskites follows expectations from classical defect chemistry, *Eur. J. Inorg. Chem.*, 2021, (28), 2882–2889.

56 M. Salado, L. Calio, R. Berger, S. Kazim and S. Ahmad, Influence of the mixed organic cation ratio in lead iodide based perovskite on the performance of solar cells, *Phys. Chem. Chem. Phys.*, 2016, **18**, 27148.

57 K. Shimamura, T. Hakamata, F. Shimojo, R. K. Kalia, A. Nakano and P. Vashishta, Rotation mechanism of methylammonium molecules in organometal halide perovskite in cubic phase: an ab initio molecular dynamics study, *J. Chem. Phys.*, 2016, **145**(22), DOI: 10.1063/1.4971791.

58 J. Li, M. Bouchard, P. Reiss, D. Aldakov, S. Pouget, R. Demadrille and C. Aumaitre, *et al.*, Activation energy of organic cation rotation in $CH_3NH_3PbI_3$ and $CD_3NH_3PbI_3$: quasi-elastic neutron scattering measurements and first-principles analysis including nuclear quantum effects, *J. Phys. Chem. Lett.*, 2018, **9**(14), 3969–3977.

59 O. Knop, R. E. Wasylishen, M. A. White, T. S. Cameron and M. J. V. Oort, Alkylammonium lead halides. Part 2. CH_3NH_3-PbX_3 (X = Cl, Br, I) perovskites: cuboctahedral halide cages with isotropic cation reorientation, *Can. J. Chem.*, 1990, **68**(3), 412–422.

60 J. Wu, J. Chen and H. Wang, Phase Transition Kinetics of MAPbI3 for Tetragonal-to-Orthorhombic Evolution, *JACS Au*, 2023, **3**(4), 1205–1212.

61 T. Baikie, Y. Fang, J. M. Kadro, M. Schreyer, F. Wei, S. G. Mhaisalkar, M. Graetzel and T. J. White, Synthesis and crystal chemistry of the hybrid perovskite $(CH_3NH_3)PbI_3$ for solid-state sensitised solar cell applications, *J. Mater. Chem. A*, 2013, **1**(18), 5628–5641.

62 D. Prochowicz, P. Yadav, M. Saliba, M. Saski, S. M. Zakeeruddin, J. Lewinski and M. Gratzel, Reduction in the interfacial trap density of mechanochemically synthesized $MAPbI_3$, *ACS Appl. Mater. Interfaces*, 2017, **9**(34), 28418–28425.

63 V. Compañ, R. Diaz-Calleja, J. Diaz-Boils and J. Escorihuela, Distribution of Relaxation Times: Debye Length Distribution vs Electrode Polarization by a Cole–Cole Relaxation Model, *J. Electrochem. Soc.*, 2022, **169**(1), 013506.

64 S. B. Aziz, W. O. Karim, M. A. Brza, R. T. Abdulwahid, S. R. Saeed, S. Al-Zangana and M. F. Z. Kadir, Ion transport study in CS: POZ based polymer membrane electrolytes using Trukhan model, *Int. J. Mol. Sci.*, 2019, **20**(21), 5265.

65 C. Krause, J. R. Sangoro, C. Iacob and F. Kremer, Charge transport and dipolar relaxations in imidazolium-based ionic liquids, *J. Phys. Chem. B*, 2010, **114**(1), 382–386.

66 T. M. W. J. Bandara, M. A. K. L. Dissanayake, O. A. Ileperuma, K. Varaprathan, K. Vignarooban and B. E. Mellander, Polyethyleneoxide (PEO)-based, anion conducting solid polymer electrolyte for PEC solar cells, *J. Solid State Electrochem.*, 2008, **12**, 913–917.

67 D. Valverde, A. Garcia-Bernabé, A. Andrio, E. García-Verdugo, S. V. Luis and V. Compañ, Free ion diffusivity and charge concentration on cross-linked polymeric ionic liquid iongel films based on sulfonated zwitterionic salts and lithium ions, *Phys. Chem. Chem. Phys.*, 2019, **21**(32), 17923–17932.

68 J. Vega-Moreno, A. A. Lemus-Santana, E. Reguera, A. Andrio and V. Compañ, High proton conductivity at low and moderate temperature in a simple family of Prussian blue analogs, divalent transition metal hexacyanocobaltates(III), *Electrochim. Acta*, 2020, **360**, 136959.

69 L. M. Herz, Charge-carrier mobilities in metal halide perovskites: fundamental mechanisms and limits, *ACS Energy Lett.*, 2017, **2**(7), 1539–1548.

70 T. Smith Sorensen, Electrodynbamics and dielectric/Impedance spectroscopy of membranes and polymers, *Encycl. Surf. Colloid Sci.*, 2002, 1796–1819. Marcel Dekker, Inc. vol. 270 Madison Avenue. New York, p. 10016.

71 S. D. Stranks, G. E. Eperon, G. Grancini, C. Menelaou, M. J. Alcocer, T. Leijtens, L. M. Herz, A. Petrozza and H. J. Snaith, Electron-hole diffusion lengths exceeding 1 micrometer in an organometal trihalide perovskite absorber, *Science*, 2013, **342**(6156), 341–344.